Soft Matter

Nanocomposite Tectons as Unifying Systems for Nanoparticle Assembly

Journal:	*Soft Matter*
Manuscript ID	SM-ART-12-2021-001738.R2
Article Type:	Paper
Date Submitted by the Author:	18-Feb-2022
Complete List of Authors:	Xia, Jianshe; Institute of Chemistry, Chinese Academy of Sciences, State Key Laboratory of Polymer Physics and Chemistry Lee, Margaret; Massachusetts Institute of Technology, Materials Science Santos, Peter; Massachusetts Institute of Technology, Materials Science Horst, Nathan; Iowa State University, MSE Macfarlane, Robert; Massachusetts Institute of Technology, Materials Science Guo, Hongxia; Institute of Chemistry, Chinese Academy of Sciences, State Key Laboratory of Polymer Physics and Chemistry Travesset, Alex; Iowa State University of Science and Technology, Physics and Astronomy

Nanocomposite Tectons as Unifying Systems for Nanoparticle Assembly

Jianshe Xia,[†,‡] Margaret Lee,[¶] Peter J. Santos,[¶] Nathan Horst,[§,‖] Robert J. Macfarlane,[¶] Hongxia Guo,[*,†,‡] and Alex Travesset[*,⊥]

† *Beijing National Laboratory for Molecular Sciences, Institute of Chemistry, Chinese Academy of Sciences, Beijing 100190, China*

‡*University of Chinese Academy of Sciences, Beijing 100049, China*

¶*Department of Materials Science and Engineering, Massachusetts Institute of Technology, 77 Massachusetts Avenue, Cambridge, Massachusetts 02139, United States*

§*Department of Materials Science and Engineering, Iowa State University, Ames, Iowa 50011, USA*

‖*Ames Laboratory, U.S. Department of Energy, Ames, Iowa 50011, USA*

⊥*Department of Physics and Astronomy and Department of Materials Science and Engineering, Iowa State University and Ames Lab, Ames, IA 50011, USA*

E-mail: hxguo@iccas.ac.cn; trvsst@ameslab.gov

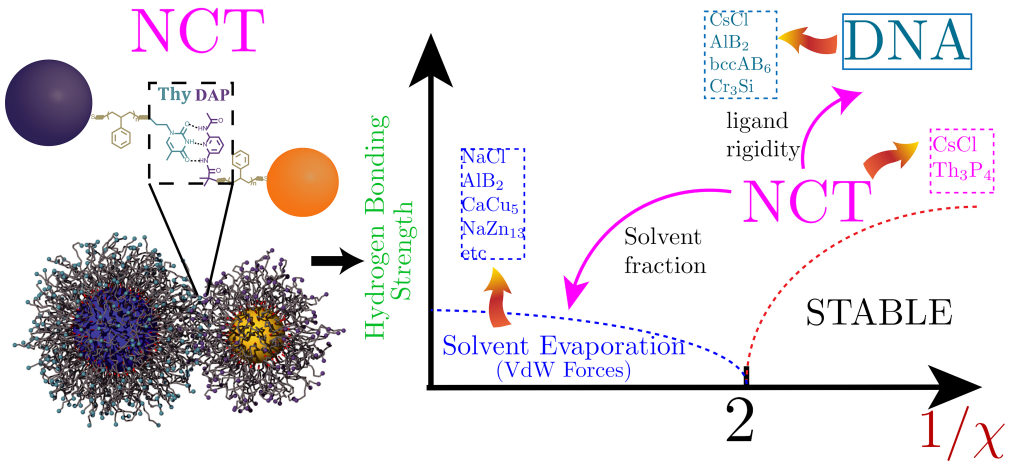

Abstract

Nanocomposite tectons (NCTs) are nanocomposite building blocks consisting of nanoparticle cores functionalized with a polymer brush, where each polymer chain terminates in a supramolecular recognition group capable of driving particle assembly. Like other ligand-driven nanoparticle assembly schemes (for example those using DNA-hybridization or solvent evaporation), NCTs are able to make colloidal crystal structures with precise particle organization in three dimensions. However, despite the similarity of NCT assembly to other methods of engineering ordered particle arrays, the crystallographic symmetries of assembled NCTs are significantly different. In this study, we provide a detailed characterization of the dynamics of hybridizations through universal (independent of microscopic details) parameters. We perform rigorous free energy calculations and identify the persistence length of the ligand as the critical parameter accounting for the differences in the phase diagrams of NCTs and other assembly methods driven by hydrogen bond hybridizations. We also report new experiments to provide direct verification for the predictions. We conclude by discussing the role of non-equilibrium effects and illustrating how NCTs provide a unification of the two most successful strategies for nanoparticle assembly: solvent evaporation and DNA programmable assembly.

Keywords

Nanoparticle, Nanocomposites, Tectons, Hydrogen Bonds, Binary systems, Assembly, X-rays.

Introduction

The two most successful strategies for synthesizing crystalline arrays of nanoparticles[1] are DNA mediated assembly[2–7] and solvent evaporation (SE) of a stable nanoparticle suspension.[8–11] Although there are some commonalities, for example the binary superlattices (BNSLs) AlB_2 or $bccAB_6$ (also known as Cs_6C_{60}) have been obtained from both strategies,[6,9,10] there are also some important differences: SE results are driven by VanDer Waals forces that gradually become attractive as solvent is evaporated, resulting in dry (solvent free) structures,[9] while DNA assembly is driven by supramolecular interactions such as hydrogen bonds and electric charges, leading to more open structures, with up to 90% of the lattice being filled with solvent (water).[41] It is therefore challenging to make connections between these two types of assembly for the purpose of developing more unifying principles in nanoparticle-based crystallization.

Recently, a new class of nanoparticle-based building block has been developed,[12–16] i.e., nanocomposite tectons (NCTs), see Fig. 1, which are nanoparticles (NPs) consisting of a core functionalized with a dense polymer brush, where each polymer chain comprising the brush terminates in a supramolecular binding group. Multiple binding groups have been used to control interparticle interactions, including hydrogen bonding, metal coordination, and dynamic covalent chemistry, providing a diverse array of ligand chemistries to tune assembly behavior. The most-studied NCT assembly processes uses a binary pair of complementary particles whose polymer chains terminate in either diaminopyridine (DAP) or thymine (Thy) groups. DAP and Thy are complementary, meaning that they exhibit a fairly strong binding

[1] while it is possible to dry samples obtained through DNA assembly, the initial structure is determined from supramolecular bonds between DNA strands.

affinity for their complement, but only weak binding affinity for other groups of the same type. Because NCTs are stable in an organic solvent and, at the same time, their assembly can be directed through hydrogen bonds, they provide an example of a system that may be assembled either as complementary ligand interactions, like DNA, or through SE. NCTs open up the exciting, yet unexplored, possibility of intermediate assembly strategies simultaneously combining SE and supramolecular bonding hybridizations. Such investigations provide more generalizable information on NP crystal formation that could help to explain differences between these two different types of superlattice formation.

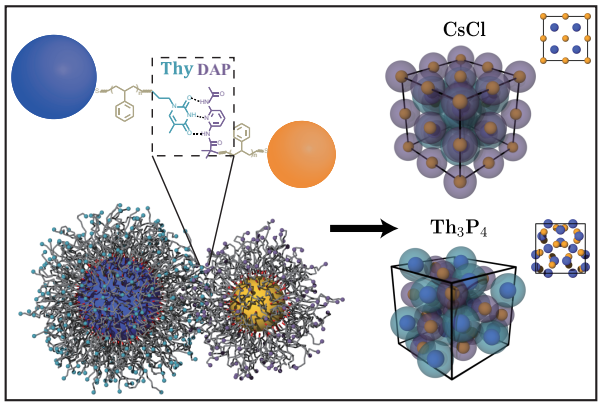

Figure 1: NCTs (left) assemble into CsCl or Th_3P_4 BNSL by the hydrogen bond hydridization between polystyrene terminated moieties, that is, DAP and Thy.

It is well established, both from experiments[6] and simulations[17–20] that the phase diagram of binary systems assembled through DNA consists of four different BNSLs in the sequence

$$\mathrm{CsCl} \rightarrow \mathrm{AlB_2} \rightarrow \mathrm{Cr_3Si} \rightarrow \mathrm{bccAB_6}\ (\mathrm{Cs_6C_{60}})\ , \tag{1}$$

for increasing NP asymmetry. Because current methods for crystallizing NCTs use a hydrogen bond-driven approach, it could be predicted that the same sequence of structures would also be obtained. Surprisingly, however, only two phases[14] have been reported (see Fig. 1) at present, namely,

$$\mathrm{CsCl} \rightarrow\ \mathrm{Th_3P_4}\ . \tag{2}$$

The apparent absence of AlB_2, Cr_3Si and bccAB$_6$ does point to a subtle dependence of the phase diagram on the molecular details of the hydrogen bond hybridization systems. The Th_3P_4 phase has been reported previously in DNA mediated assembly, either in binary systems of proteins and nanoparticles[21] or assemblies using "multivalent" DNA strands that incorporate organic branching points along the DNA backbone;[22] both of these assemblies have different DNA distribution across the NP surfaces than would be expected for the traditional systems used to make the BNSL sequence in Eq. 1

The primary goals of this paper is to characterize the equilibrium structures and dynamics for nanoparticle assembly driven by hydrogen bonding in terms of experimentally tunable physical parameters, and explain the differences with assembly by SE.[23,24] We will achieve these goals by examining NCTs as intermediate systems that bridge the supramolecular DNA and SE strategies. Specifically, a binary NCT system with passivated hydrogen bonding, all Thy (or DAP) for example, is basically just a NP core functionalized with polystyrene, which has already been demonstrated, both from experiment[10] and theory[25–28] to assemble by SE into the rich diverse phases as reported with short hydrocarbon chains.

We therefore formulate a rigorous coarse-grained (CG) model and validate it by comparing with both previously published and newly collected experimental data. We then investigate the dynamics of assembly and identify different quantities that are independent of the details of the interaction. Through precise free energy calculations, we determine the stability of the different phases and validate our model, both quantitatively and qualitatively, against assembly experiments.

Coarse-Grained Model

Model Parameters

A NCT is composed of a rigid core with polystyrene (PS) chains consisting of n_{PS} monomers grafted to the core surface with grafting density σ_g. The free ends of PS are functionalized

with either DAP or Thy groups. In the actual experiments,[12–14] the physical dimensions of the core vary in a range between 10 to 50 nm when functionalized with PS with molecular weights in the range of 3.7-18.5 kDa, or $n_{PS} = 36 - 178$ monomers (the molar mass $M_w = 104.15$ Da/mol for a PS unit has been used), see Table 1. The Kuhn length for PS is $b = 20 - 25$Å and the limit characteristic ratio $C_\infty = 10 - 14$.[27,29] We therefore take $b = 20$Å and $C_\infty = 10$. Then, the number of Kuhn segments N is

$$L = r_0^{PS} \cos(\alpha/2) n_{PS} = Nb \rightarrow N = \frac{r_0^{PS} \cos(\alpha/2)}{b} n_{PS} \approx 0.18 n_{PS} \ , \tag{3}$$

where L is the maximum polymer length, the average bond length $r_0^{PS} = 4.9$ Å, and the average bond angle $\alpha = 88.15$.[27] Within the coarse-grained model, NCT consists of a rigid core and n effective PS beads (with diameter $\sigma = 1.12$ nm, see the supporting information) connected with harmonic bonds set to $r_0 = 0.84\ \sigma$. The DAP/Thy groups are connected to the end bead by harmonic bonds with $r_0 = 0.63\ \sigma$. As shown in the supporting information (SI)

$$N = 0.47n \rightarrow n = 0.38 n_{PS}. \tag{4}$$

As a cross-check to Eq. 3 and Eq. 4 we plot the hydrodynamic radius as measured by dynamic light scattering (DLS)[14] vs the one obtained from simulations.

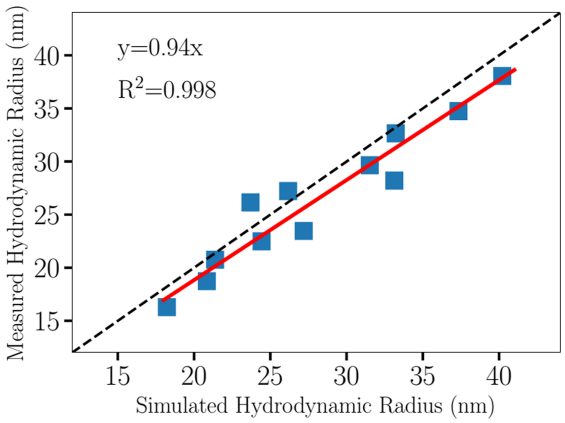

Figure 2: Comparison of hydrodynamic radius of individual NCTs for the experiments[14] and our simulations (calculated as the average value of the maximums of the distances for all the particles in per ligand chain from the NP center in a single isolated NCT) with parameters derived from Eq. 4 (grafting density is slightly dependent on the NCT samples,[14] but it is around 0.5 chains/nm^2). The black dashed line is the one-to-one matched line for the experimental hydrodynamic radius and the simulated one. The solid red line is the linearly fitting with R-Square=0.998. (Simulations data for this case included more general NCTs than those in Table 2).

Hybridization between complementary DAP-Thy is implemented through Lennard-Jones (LJ) potentials between coarse-grained hydrogen bond acceptors (A) and donors (B). In order to prevent un-physical multiple hybridizations on a given site, "flanking beads" are introduced, see Fig. 3, along the same lines of previous models describing DNA-mediated nanoparticle assemblies.[17] The entire DAP/Thy moiety is therefore represented as 4 flanking beads and one central A or B bead. Explicit force field parameters are given in Tables S1,S2,S3.

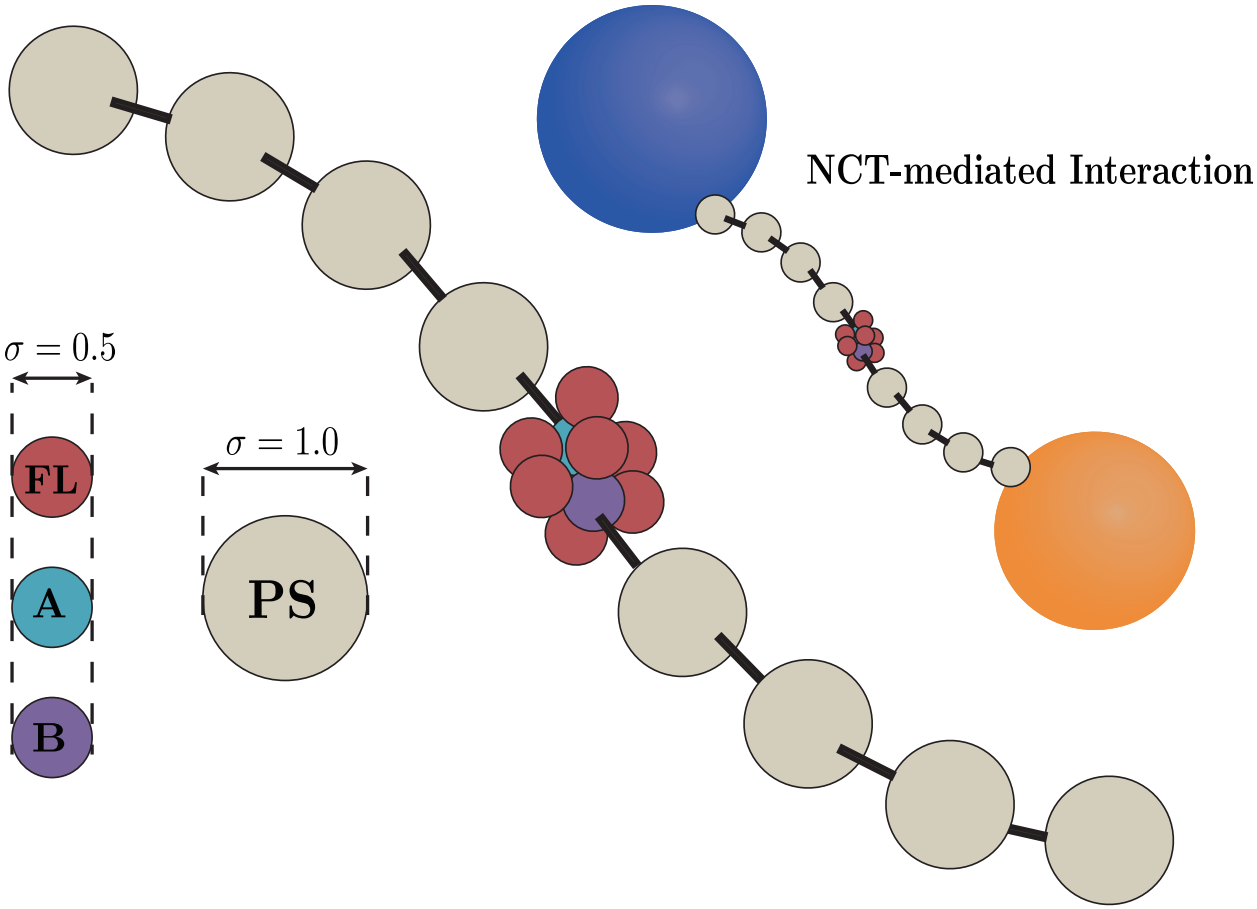

Figure 3: Coarse-grained model for NCT-mediated interactions, where flanking beads mediate specific interactions between complementary "A-B" NCTs.

Table 1: Mapping into physical units: NCTs in the work are denoted as NP1 to NP9, R_c is the NP core radius, n_{PS} is the number of PS monomers, MW is molecular weight and σ_g is the actual grafting density.

	R_c(nm)	n_{PS}	MW(kDa)	σ_g (chns/nm^{-2})
NP1	3.36	21	2.2	0.4
NP2	4.48	21	2.2	0.4
NP3	5.04	21	2.2	0.4
NP4	5.60	21	2.2	0.4
NP5	7.84	21	2.2	0.4
NP6	10.08	21	2.2	0.4
NP7	5.00	32	3.3	0.5
NP8	7.00	32	3.3	0.5
NP9	7.50	32	3.3	0.5

NPs, i.e., NCTs here, are suspended in toluene, which is a good solvent for PS. Here,

the solvent is considered implicitly by a generic molecular dynamics (MD) model outlined in SI, see Fig. S1, where we have determined that $T = 4$ (in units of $\varepsilon = 1$, see Table S1) corresponds to good solvent conditions.

The MD simulations are performed by setting a temperature $T = 4 \equiv T_m$ and tuning the A and B attraction ε_{AB}. As described in Ref.,[17] ε_{AB} must be chosen large enough so that there is an attraction between complementary NPs, but not so large that the hybridization times exceed the duration of the entire simulation, which would lead to a quenched system. We define a hybridization to occur whenever A-B beads are within a distance of $2\sigma_{AB}$, where the interaction energy is about 6% of the maximum well depth.

It is useful to define the effective hard sphere (HS) radius/diameter for a NCT, which as discussed in Ref.[30] is given by the optimal packing model (OPM)[31] formula

$$r_{HS} = (1 + 3\xi\lambda)^{1/3} R_c \quad , \quad d_{HS} = 2r_{HS} \tag{5}$$

where $\lambda = \frac{L}{R_c}$ and $\xi = \frac{\sigma_g}{\sigma_{g,Max}}$, where here the maximum CG PS extension length $L = 0.84n + 0.63$ (σ), see Table 2, R_c is the NP core radius, $\sigma_{g,Max}$ is the maximum grafting density and $\sigma_{g,Max} = 1$ chains/$\sigma^2 \approx 0.8$ chains/nm^2 is considered throughout the paper. To characterize binary systems consisting of NPs with different sizes, we introduce the parameter

$$\gamma = \frac{r_{HS}^B}{r_{HS}^A} \ , \tag{6}$$

that is, the ratio of the two effective HS radius for the smallest NP B and the largest NP A.

Computational Details

The BNSLs are built according to the parameters specified in the HOODLT package[25,32] for the given values of γ, see Eq. 6. The potential of mean force (PMF) is computed from the

Table 2: NP Parameters: Molecular Weight (MW), Core Diameter $2R_c$, the Number of CG PS Repeating Units n, the Number of Grafted PS Chains m, the Maximum Extension of the Ligand L (σ), NP Effective Hard Sphere Diameter $d_{HS} = 2r_{HS}$ (σ) (See Eq. 5) and the Hydrodynamic Radius $r^H_{i,m}$ (σ).

NP	MW (kDa)	$2R_c$ (nm/CG)	n	m	L (σ)	d_{HS} (σ)	$2r^H_{i,m}$ (σ)
NP1	2.2	6.72/6	8	57	7.35	10.03	14.25
NP1_1	3.3	6.72/6	12	57	10.71	11.11	16.56
NP1_2	4.4	6.72/6	16	57	14.07	12.02	18.55
NP1_3	6.6	6.72/6	24	57	20.79	13.50	21.79
NP1_4	9.9	6.72/6	36	57	30.87	15.25	25.76
NP1_5	13.2	6.72/6	48	57	40.95	16.68	29.92
NP1_6	16.4	6.72/6	60	57	51.03	17.89	32.63
NP2	2.2	8.96/8	8	101	7.35	12.44	16.56
NP2_1	3.3	8.96/8	12	101	10.71	13.69	18.96
NP2_2	4.4	8.96/8	16	101	14.07	14.76	20.97
NP3	2.2	10.08/9	8	127	7.35	13.60	18.42
NP4	2.2	11.2/10	8	157	7.35	14.74	18.84
NP4_1	3.3	11.2/10	12	157	10.71	16.15	21.40
NP4_2	4.4	11.2/10	16	157	14.07	17.35	23.56
NP5	2.2	15.68/14	8	308	7.35	19.19	23.15
NP5_1	3.3	15.68/14	12	308	10.71	20.83	25.96
NP5_2	4.4	15.68/14	16	308	14.07	22.25	28.41
NP6	2.2	20.16/18	8	509	7.35	23.50	27.42
NP7	3.3	10/8.92	12	157	10.71	15.78	20.74
NP8	3.3	14/12.5	12	308	10.71	20.21	25.04
NP9	3.3	15/13.4	12	353	10.71	21.27	26.09

weighted histogram analysis method (WHAM),[33] see also Ref.[34] Molecular dynamics (MD) simlations were carried out by HOOMD-Blue[35] using rigid body dynamics.[36] The free energy is calculated by adding a harmonic term to connect the nearest (and occasionally, next to nearest) neighbor NPs,[37] which has the form as follows

$$W = \frac{k}{2}\left(|\mathbf{r}_j - \mathbf{r}_l| - |\mathbf{R}_j - \mathbf{R}_l|\right)^2 \ , \tag{7}$$

where $\mathbf{r}_j, \mathbf{r}_l$ indicate the positions of the nearest neighbors, and $\mathbf{R}_j, \mathbf{R}_l$ their positions in the zero temperature defect free lattice. The free energy is obtained by integrating[38]

$$\frac{\partial F(T;k,a_L)}{\partial a_L} = -\frac{3N}{\beta a_L} + \frac{2}{a_L}\langle W\rangle - 3\frac{V}{a_L}P(a_L) \ , \tag{8}$$

where $P(a_L)$ is the pressure, see Ref.[38] for a detailed discussion, at the corresponding lattice constant a_L with the harmonic term excluded, and $\langle W\rangle$ is the average of the harmonic term, that is

$$F(T;k,a_L) - F(T;k,a_L^0) = \int_{a_L^0}^{a_L} dx \frac{\partial F(T;k,a_L)}{\partial x} \ . \tag{9}$$

where a_L^0 is chosen sufficiently large so that the free energy contains contributions from the harmonic terms only. In a typical run, NPs were equilibrated with $(1-2)\times 10^7$ time steps before data collection, which was performed per 1000-5000 time steps and consisted of roughly $(5-10)\times 10^6$ time steps. Some larger systems ran longer time. We typically ran 9-14 windows with different a_L values.

Experiments

Materials and Characterization Methods

2,6-Diaminopyridine, thymine, acetyl chloride, 11-bromoundecan-1-ol, 2-bromoisobutyryl bromide, styrene, N,N,N′,N″,N‴-pentamethyldiethylenetriamine (PMDETA),

tris[2-(dimethylamino)ethyl]amine(Me_6TREN), and basic alumina were purchased from Fisher Scientific. Copper bromide was purchased from Sigma Aldrich. Aminoethanethiol was purchased from TCI America. Hydrogen tetrachloroaurate(III) trihydrate was purchased from Beantown Chemical. General solvents were purchased from Fisher Scientific. All chemicals, including solvents, were used without further purification, except styrene, which was passed through a short column of basic alumina to remove inhibitor prior to polymerization. Note that some solvents were purchased as anhydrous grade.

Centrifugation was performed with an Eppendorf 5424 centrifuge. ^{1}H NMR spectra were obtained on a Varian 300 MHz instrument. Gel permeation chromatography (GPC) characterizations were performed on an Agilent Technologies GPC system, with THF as the eluent at 1.0 mL/min, and monodisperse polystyrene as the standard. UV-vis spectra and measurements were obtained on a Cary-500 or Cary-50 Bio spectrometer. Small angle x-ray scattering (SAXS) measurements were performed at the 12ID-B station at the Advanced Photon Source (APS) at Argonne National Laboratory. The samples were probed using 14 keV (0.8856 Å) X-rays, and the sample-to-detector distance was calibrated with a silver behenate standard. The beam was collimated using two sets of slits, and a pinhole was used. Scattered radiation was detected using a Pilatus 2 M detector.

NCT Synthesis

The synthesis of the DAP and Thy initiators has been previously reported.[39] The DAP polymers were synthesized by activator regenerated by electron transfer atom transfer radical polymerization (ARGET-ATRP) of polystyrene using an initiator modified with a DAP moiety.[15] The Thy polymers were synthesized by ATRP of polystyrene using initiators containing a Thy moiety as previously reported.[12] Polymers were characterized by gel permeation chromatography (GPC), and their molecular weights and dispersities are summarized in Table S14. After polymerization, the terminal bromine atom of polymers were modified with aminoethanethiol, as described previously.[12]

Citrate-capped gold NPs were synthesized by a literature procedure[40] slightly modified.[14] NPs were characterized with transmission electron microscopy (TEM). Their sizes and distributions are summarized in Table S15.

Au-NCTs were synthesized as previously reported.[12] In brief, a solution of as-synthesized gold NPs was added to an equal volume of 1 mg ml^{-1} thiolated DAP or Thy polystyrene, and was vigorously shaken for 1 min. The resulting pink precipitate was collected by gentle centrifugation and redispersed in N,N-dimethylformamide (DMF). The NCTs were then subjected to a series of three centrifuge cycles, redispersing in DMF, toluene, and toluene. Centrifuge protocols were determined by particle size, and are listed in Table S15. The concentration of the NCTs was measured using Beer's Law, and adjusted to match the desired concentration for the experiment.

NCT Crystallization

To prepare crystalline Au-NCT assemblies, equal volumes of purified DAP and Thy NCTs were combined in a PCR tube. After assembly, samples were heated to above their melting temperature and annealed by slow cooling in a Techne Prime Thermal Cycler at an inverse cooling rate of 1 min per 0.1 °C.

Small Angle X-Ray Scattering (SAXS) of Assembled NCTs

SAXS samples were loaded into a short section of 1.5-mm diameter polyimide tubing (Cole-Parmer) and sealed at both ends with epoxy. Before loading samples into the tubing, one end was sealed with epoxy and the tubing was baked at 110 °C overnight. Crystal structures were determined by peak indexing. The lowest q peak identified in SAXS (q_0) was fit using a pseudo-Voight function, and the lattice parameter a was determined as:

$$a_{\mathrm{BCC}} = \frac{2\pi\sqrt{2}}{q_0}, \quad a_{\mathrm{CsCl}} = \frac{2\pi}{q_0}, \quad a_{\mathrm{Th_3P_4}} = \frac{2\pi\sqrt{6}}{q_0} \ . \tag{10}$$

For completeness, some SAXS experimental data are shown in SI, Fig. S20, Fig. S21 and Fig. S22.

Results and Discussion

All results in this section correspond to the temperature $T = 4 \equiv T_m$, i.e., in good solvent conditions, as justified above.

Potential of Mean Force

The PMF shown in Fig. 4 confirms that the DAP-Thy hybridizations induce NP attraction for $\frac{\varepsilon_{AB}}{k_B T_m} \gtrsim 10$, with an equilibrium distance R_{eq} which is a monotonic decreasing function of $\frac{\varepsilon_{AB}}{k_B T_m}$.

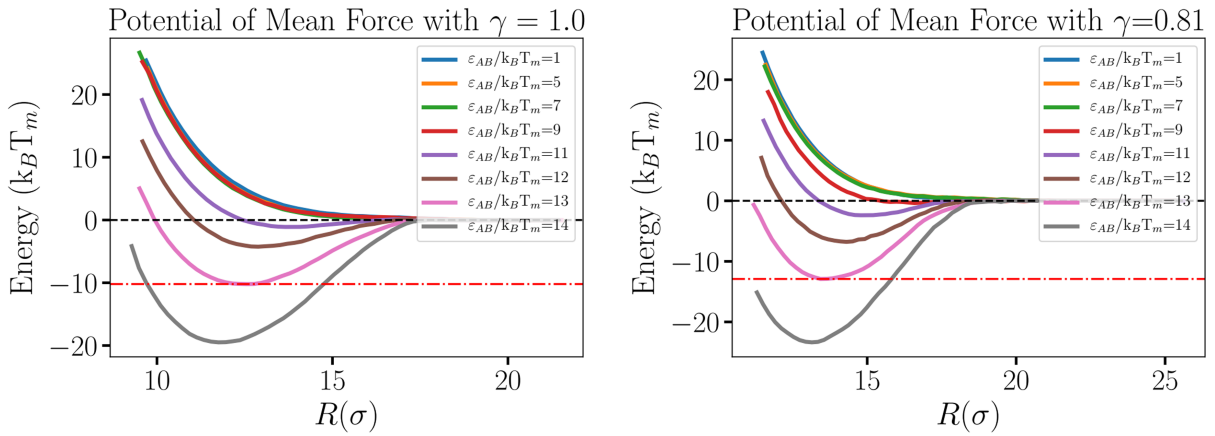

(a) (b)

Figure 4: Potential of mean force as a function of the NCT hybridization strength ($\varepsilon_{AB}/k_B T_m$) for (a) $\gamma = 1$ (NP1 - NP1) and (b) $\gamma = 0.81$ (NP2 - NP1), where the red dashed line means the minimum of PMF for $\varepsilon_{AB}/k_B T_m = 13.0$.

The optimal value of $\frac{\varepsilon_{AB}}{k_B T_m}$ is determined by taking a CsCl BNSL as an example. We first calculate the fraction of hybridizations $f_H(t)$ that remains up to a time t, with results shown in Fig. 5 (a). Rather interestingly, these results are collapsed into a universal curve

as illustrated in Fig. 5 (b) by rescaling the time t as below

$$f_H(t) \approx F\left(\frac{t}{\tau}\right), \quad \tau = \tau_0 \left(e^{\frac{\varepsilon_{AB}}{k_B T_m}}\right)^{\alpha} \tag{11}$$

which implies the mean lifetime $t_{1/2}$ (defined where there are 50% hybridizations) in a stretched exponential dependence on $\frac{\varepsilon_{AB}}{k_B T_m}$

$$t_{1/2} = c\tau = c\tau_0 \left(e^{\frac{\varepsilon_{AB}}{k_B T_m}}\right)^{\alpha} \tag{12}$$

where $c = F^{-1}(\frac{1}{2}) = 0.64$, $\tau_0 = 0.015$, $\alpha = 0.72 \approx \frac{3}{4}$ for the CsCl BNSL with NP1 as indicated in the upper plot of Fig.5 (c).

The average number of hybridizations $\langle p_H \rangle$ is presented in the lower plot of Fig. 5 (c). It shows some similarities with recent calculations on DNA systems,[41] but instead, we find a more complex function, which is attributed to the flexibility of the polymer ligands as described in our study. Additionally, as illustrated in Fig. 5(d), the minimum of the free energy F_{min} and the corresponding nearest neighbor distance d_{AB} vary linearly with $\varepsilon_{AB}/k_B T_m$ when $\varepsilon_{AB}/k_B T_m > 13.0$ for the CsCl lattices with NP1.

Following Ref.[17] we can now determine the value of $\varepsilon_{AB}/k_B T_m$. Note that ε_{AB} represents a coarse-grained free energy difference: that is, the difference between the free energy of a certain number of DNA groups forming hydrogen bonds taking the free energy of the same groups with water as a reference state. This free energy depends on the actual sequence of base pairs and many other variables, so in general it is very difficult to determine its value. Fortunately, such determination is not necessary: T_c is the critical temperature where assembly takes place, so the ratio $\varepsilon_{AB}/k_B T_c$ can be determined from the simulation, as the value where the liquid→ solid phase transition occurs. In general, however it is not necessary to determine this ratio with great precision, as any value $\varepsilon_{AB}/k_B T_c < \varepsilon_{AB}/k_B T_m$ small enough that the system does not quench into an out of equilibrium gel will work. Combining with the simulated results above, the value $\varepsilon_{AB}/k_B T_m = 13$ was chosen this way.

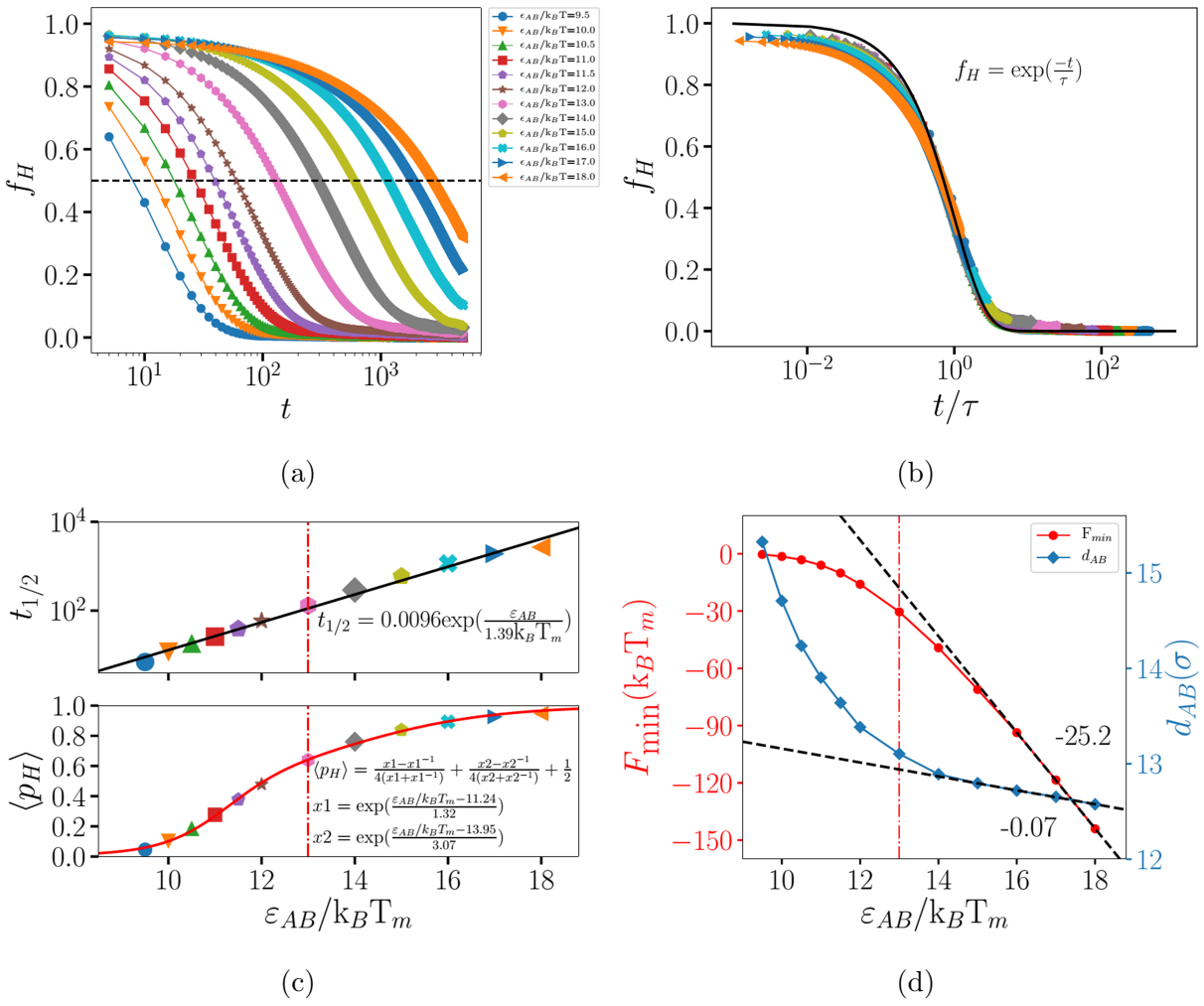

Figure 5: (a) The fraction of hybridizations f_H that lives up to a time t for different values of ε_{AB}, where the black dashed line is $f_H = 0.5$; (b) The hybridizations are collapsed into a single universal function as described in Eq. 11; (c) The mean lifetime of a hybridization is described by Eq. 12. Also shown, the average percent of hybridizations as a function of ε_{AB}; (d) The minimum of the free energy F_{min} and the corresponding nearest neighbor distance d_{AB} vary with ε_{AB}, where $F_{\min}$ and d_{AB} change linearly as $\varepsilon_{AB}/k_BT_m > 13.0$ and the black dashed lines in (c) are the linear fitting with the slope of -0.07 and -25.2. All plots correspond to the CsCl lattices with NP1. The red dashed lines represent the results for $\varepsilon_{AB}/k_BT_m = 13.0$.

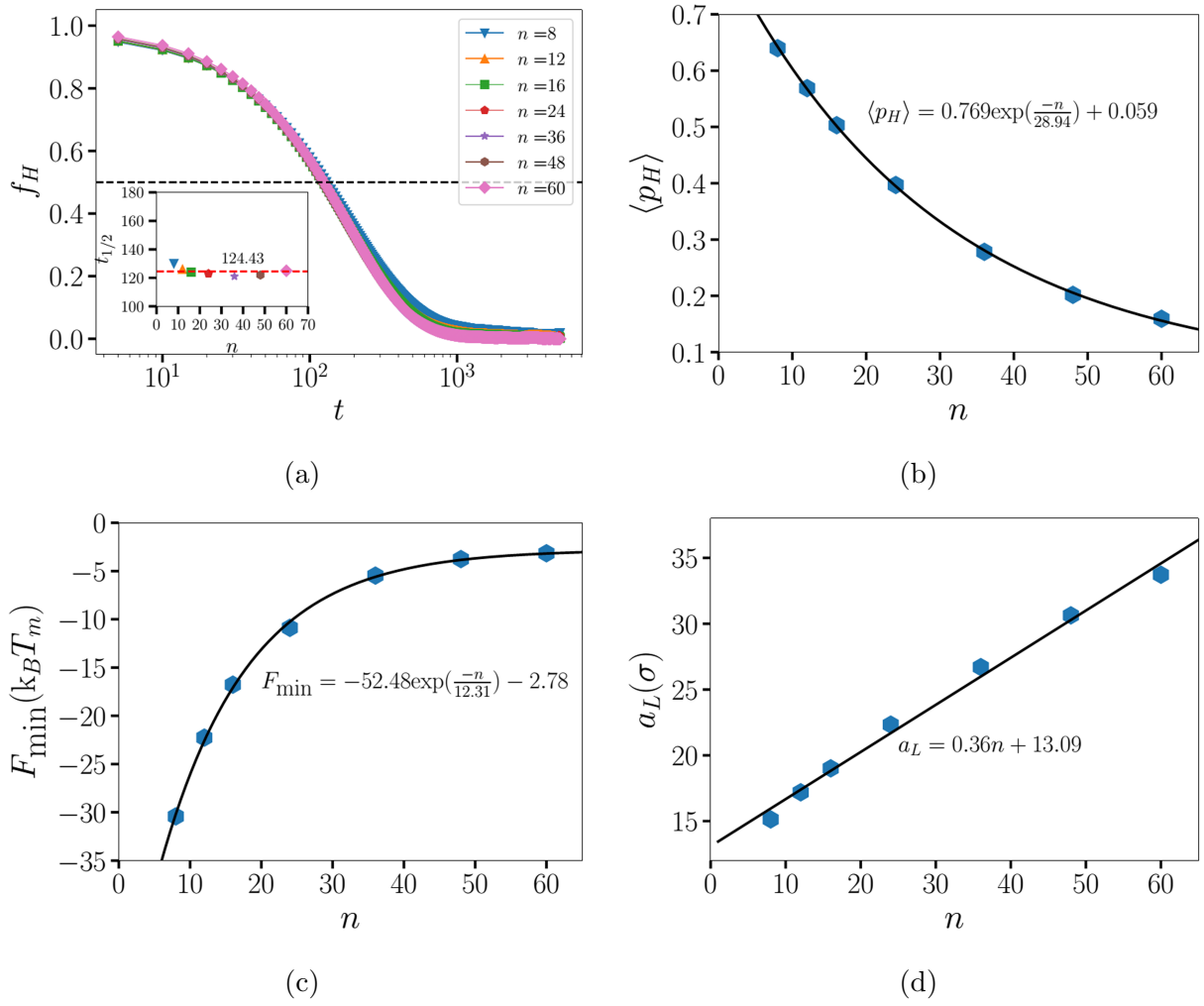

Figure 6: (a) The fraction of hybridizations f_H that lives up to a time t for different chain length n, where the black dashed line represents $f_H = 0.5$. The inset shows that the mean lifetime of a hybridization obtained by $f_H(t_{1/2}) = 0.5$ vs n; (b) The average percent of hybridizations $\langle p_H \rangle$ as a function of the chain length n; (c) The minimum of the free energy F_{min} and (d) the corresponding lattice constant a_L vary linearly with n. All plots correspond to the CsCl lattices at $\frac{\varepsilon_{AB}}{k_B T_m} = 13.0$ with the core size $2R_c = 6\sigma$, see Table 2.

The formulas of Eq. 11 and Eq. 12 are independent of chain length n, which is verified by our results on different chain length, see Fig. 6(a). The average percent of hybridizations $\langle p_H \rangle$ and the minimum of the free energy for the CsCl lattice with the core diameter $2R_c = 6\sigma$ decrease exponentially with the growth of the chain length n, and the corresponding lattice constant varies linearly with n, as shown in Fig. 6(b)-(d). The dependence of the results on the core size are further elaborated in SI. As shown in Fig. S2(a) and (b), the variation of the

fraction of hybridizations f_H with time t collapses well for the CsCl lattice with different core sizes, which implies that the formulas of Eq. 11 and Eq. 12 are also unaffected by the core sizes. Moreover, the minimum of the free energy per chain F_{min}/m and the average percent of hybridizations $\langle p_H \rangle$ for the CsCl lattice are independent of the core size for the same chain length, see Fig. S2(c). The corresponding lattice constant a_L also changes linearly with the core size $2R_c$, as illustrated in Fig. S2(d).

Superlattice Free Energy

We consider BNSLs with N_A A and N_B B NPs, and report the free energy in the dimensionless form

$$\begin{aligned} f_{\mathrm{A}_p\mathrm{B}_q} &= \frac{F_{BNSL}}{k_B T_m (N_A + N_B)} \\ \Delta f_{\mathrm{A}_p\mathrm{B}_q} &= f_{\mathrm{A}_p\mathrm{B}_q} - \frac{p}{p+q} f_{\mathrm{A}} - \frac{q}{p+q} f_{\mathrm{B}} \end{aligned} \tag{13}$$

so that $f_{\mathrm{A}_p\mathrm{B}_q}$ is the free energy per NP. Here $f_{A/B}$ are reference states for the single component A/B superlattice. Those BNSLs are not stable in the absence of hybridizations, so we set $f_A = f_B = 0$ as our reference state. Thus, a negative free energy implies a stable BNSL and we hence identify the BNSL with the lowest free energy as the equilibrium state. We also report the internal energy U and entropy $S = \frac{U-F}{T}$ for each BNSL. Note that because free energies are calculated at zero pressure (at the minimum), the Gibbs free energy has the same value as the (Helmholtz) free energy.

Each BNSL competes against a possible amorphous gel with the same stoichiometry for thermodynamic stability. For example, theoretical calculations[42] show that for single stranded DNA systems at $\gamma = 1$, the stability of the CsCl BNSL over the amorphous gel is provided by the higher entropy of the former, as there is no appreciable change in internal energy during the nucleation process. It is beyond the scope of this study to provide the detailed characterization of the amorphous gel necessary to further calculate its free energy,

which prevents us from a rigorous calculation of coexistence regions and subsequent tie lines. Therefore, we report approximate phase diagrams by assuming that the BNSL with the lowest value of $\Delta f_{\mathrm{A}_p\mathrm{B}_q} < 0$ is the stable phase, as it has been assumed in all previous studies.[6]

We also compute NP separations. Here, we denote as a_L the lattice constant and the separation between bonded NPs as $d^{A,B}$. It is also of interest to quantify the magnitude of many body effects. We therefore compute the potential of mean force (PMF) $W_{2B}(i,j)$, and evaluate the free energy of BNSL according to

$$F_{BNSL,2B} = \sum_{a=1}^{\text{all unit cells}} \sum_{i_a=1}^{i_a} \sum_{j_a=1} W_{2B}(i_a, j_a) \ , \tag{14}$$

then, many body effects are quantified according to

$$\Delta_{MB} = f_{\mathrm{A}_p\mathrm{B}_q} - f_{\mathrm{A}_p\mathrm{B}_q,2B} \ . \tag{15}$$

so that $\Delta_{MB} = 0$ represents a system entirely described by pair PMFs. Note that the sum in Eq. 14 contains both attractive (T) terms, with negative free energies ($A-B$), as well as repulsive (R) ones where free energies are positive ($B-B$ and $A-A$), so that

$$f_{A_qB_p,2B} = f^T_{A_qB_p} + f^R_{A_qB_p} \ , \tag{16}$$

then, the overall percentage of repulsive contributions is reported as

$$f_r = \frac{f^R_{A_qB_p}}{|f^T_{A_qB_p}| + f^R_{A_qB_p}} \ . \tag{17}$$

A free energy calculation for five types of BNSLs (CsCl, $\mathrm{Th_3P_4}$, $\mathrm{AlB_2}$, $\mathrm{Cr_3Si}$ and bcc$\mathrm{AB_6}$ whose symmetry space groups are $Pm\bar{3}m$, $I\bar{4}3d$, $P6/mmm$, $Pm\bar{3}n$ and $Im\bar{3}m$, respectively) for a typical binary NCTs of NP4-NP1 ($\gamma = 0.68$) is shown in Fig. 7. Generally, the free

energies are well described by two body potentials, see Eq. 14, except near the minimum. Also, the bccAB$_6$ BNSL is not stable for $\gamma = 0.68$. Additional calculations, found in SI, Fig. S3, S4, S5, S6, S7 show the same features.

The free energies and other characteristics of the BNSLs as a function of the NCT asymmetry are presented in Fig. 8. The stability of the BNSL is summarized by

$$\mathrm{CsCl} \overset{\gamma\approx 0.8}{\rightarrow} \mathrm{Th_3P_4} \overset{\gamma\approx 0.7}{\rightarrow} \mathrm{AlB_2} \overset{\gamma\approx 0.5}{\rightarrow} \mathrm{Cr_3Si} \overset{\gamma\approx 0.4}{\rightarrow} \mathrm{bccAB_6}\ . \tag{18}$$

Thus, for this set of parameters, the CsCl becomes progressively unstable when the diameters of the NPs become more dissimilar, but other BNSLs like AlB$_2$, Cr$_3$Si and bccAB$_6$ eventually become more stable. As Fig. 8 shows, the delicate balance between favorable hybridizations (internal energy) and repulsions (entropy) determines the thermodynamic state.

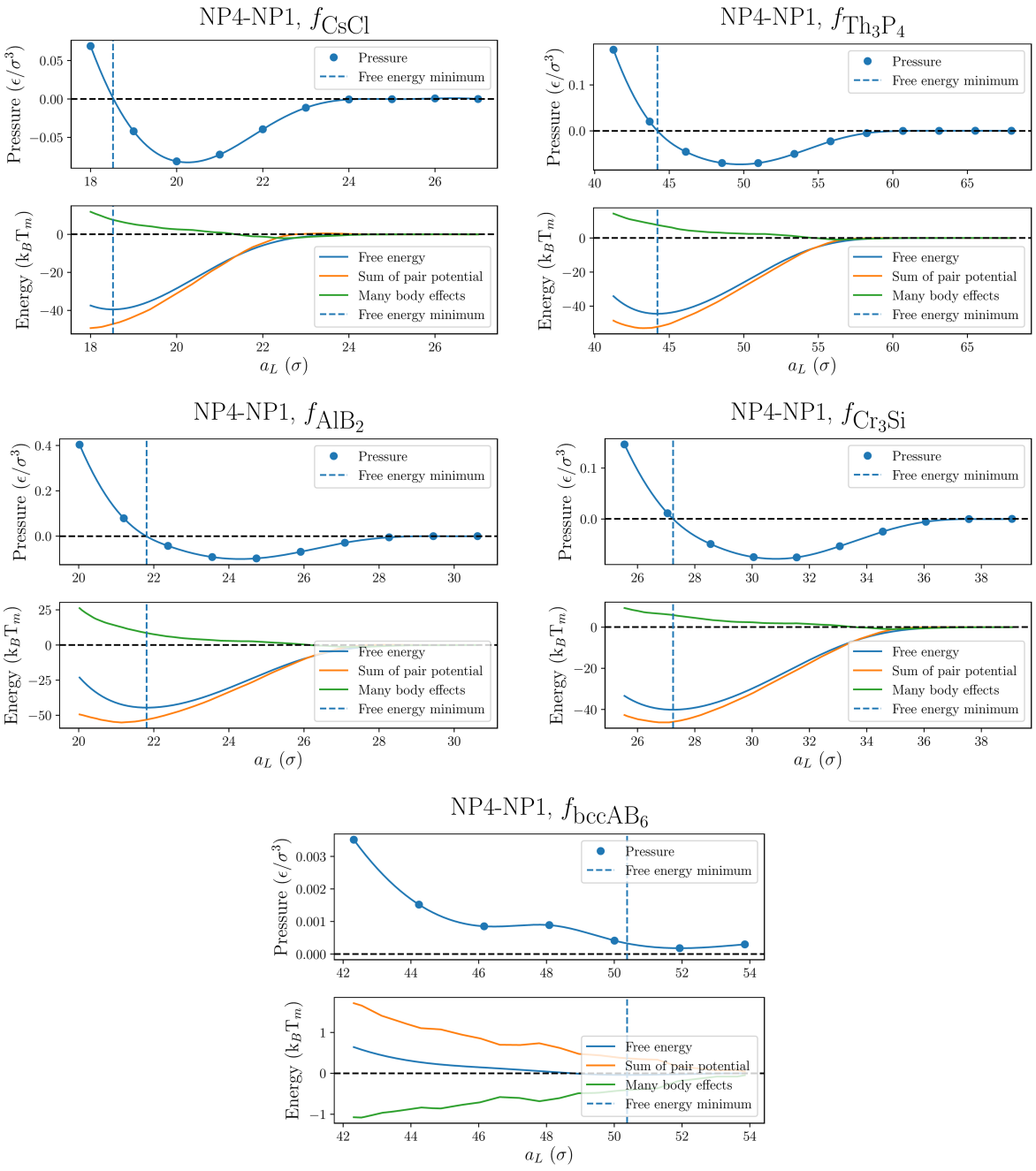

Figure 7: Pressure and free energy vs lattice constant for the BNSL CsCl, Th_3P_4, AlB_2, Cr_3Si and $bccAB_6$ with NP1 and NP4 normalized to the number of NPs within the unit cell.

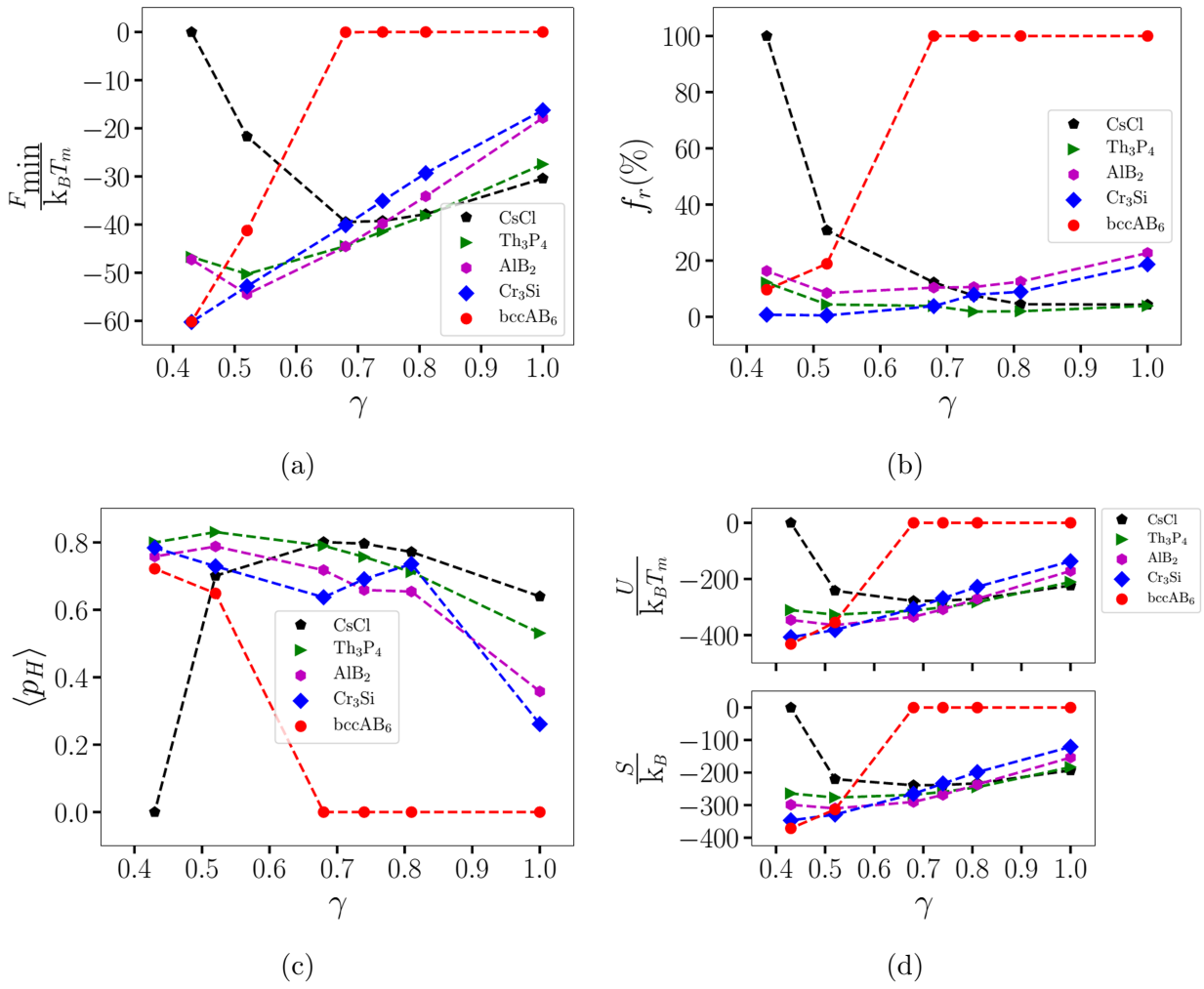

Figure 8: (a) Free energies of CsCl, Th_3P_4, AlB_2, Cr_3Si and $bccAB_6$ lattices vs γ;(b) Repulsive fraction f_r (see Eq. 17); (c) The average percent of hybridizations $\langle p_H \rangle$; (d) The internal energy $\frac{U}{k_B T_m}$ and entropy $\frac{S}{k_B}$ vs γ, see Table 2 for detailed values. All values are for $\frac{\varepsilon_{AB}}{k_B T_m} = 13.0$.

The Effect of Chain Rigidity

We consider now the effect of chain rigidity by adding a harmonic angle term

$$V(\theta) = \frac{k_\theta}{2}(\theta - \theta_0)^2 \ , \tag{19}$$

The new parameter k_θ introduces a finite persistence length so that $k_\theta \to 0$ is the case considered so far (flexible) and $k_\theta >> k_B T$ and $\theta_0 = \pi$ parameterize a rigid rod.

The PMF for a typical NCT pair (NP3-NP3), see Fig. 9(a), illustrates that repulsions are reduced with increasing chain rigidity and the same is true for other cases, i.e., NP1-NP1 and NP7-NP7, see Fig. S10. This is also apparent from Fig. 9(c), where the repulsive fractions f_r (see Eq. 17) for different BNSLs at $\gamma = 0.74$ are shown. Concurrent with the weakening of repulsions as indicated by Fig. 9(b), the Th_3P_4 BNSL becomes metastable (around $k_\theta \approx 20$) in favor of AlB_2, the expected equilibrium phase in DNA guided assembly.[6] The same trends also occur for $\gamma = 0.81$, see Fig. S12(b), but instead, the stable phase is CsCl, also in agreement with DNA guided assembly. Rather interestingly, the CsCl BNSL keeps a significant larger number of hybridizations, as shown in Fig. S12(d), which is consistent with the simulated results for BNSLs derived by DNA mediated assembly.[19] In Fig. 11 and Fig. 12, see also Fig. S14 and Fig. S15, we show that the same results hold for larger NP cores and higher grafting density, i.e., NP7, NP8 and NP9, see Table 1 and 2.

Actual free energy calculations for BNSLs are available in Fig. S11, and a more detailed analysis for free energies, internal energies, entropy, the average percent of hybridizations $\langle p_H \rangle$ and the repulsive fraction f_r as a function of the spring parameter k_θ of the harmonic angle potential for the BNSL CsCl, Th_3P_4, AlB_2 and Cr_3Si is shown in Fig 10 for $\gamma = 0.74$, with $\gamma = 0.81$ relegated to SI, see Fig. S13. Perhaps the most notable aspect is that all BNSLs exhibit a minimum in the average number of hybridizations. This minimum coincides with a maximum in the entropy as there are less "mobile" parts. The reduction of the repulsion by the increased rigidity leads, in turn, to a reduction in the free energy.

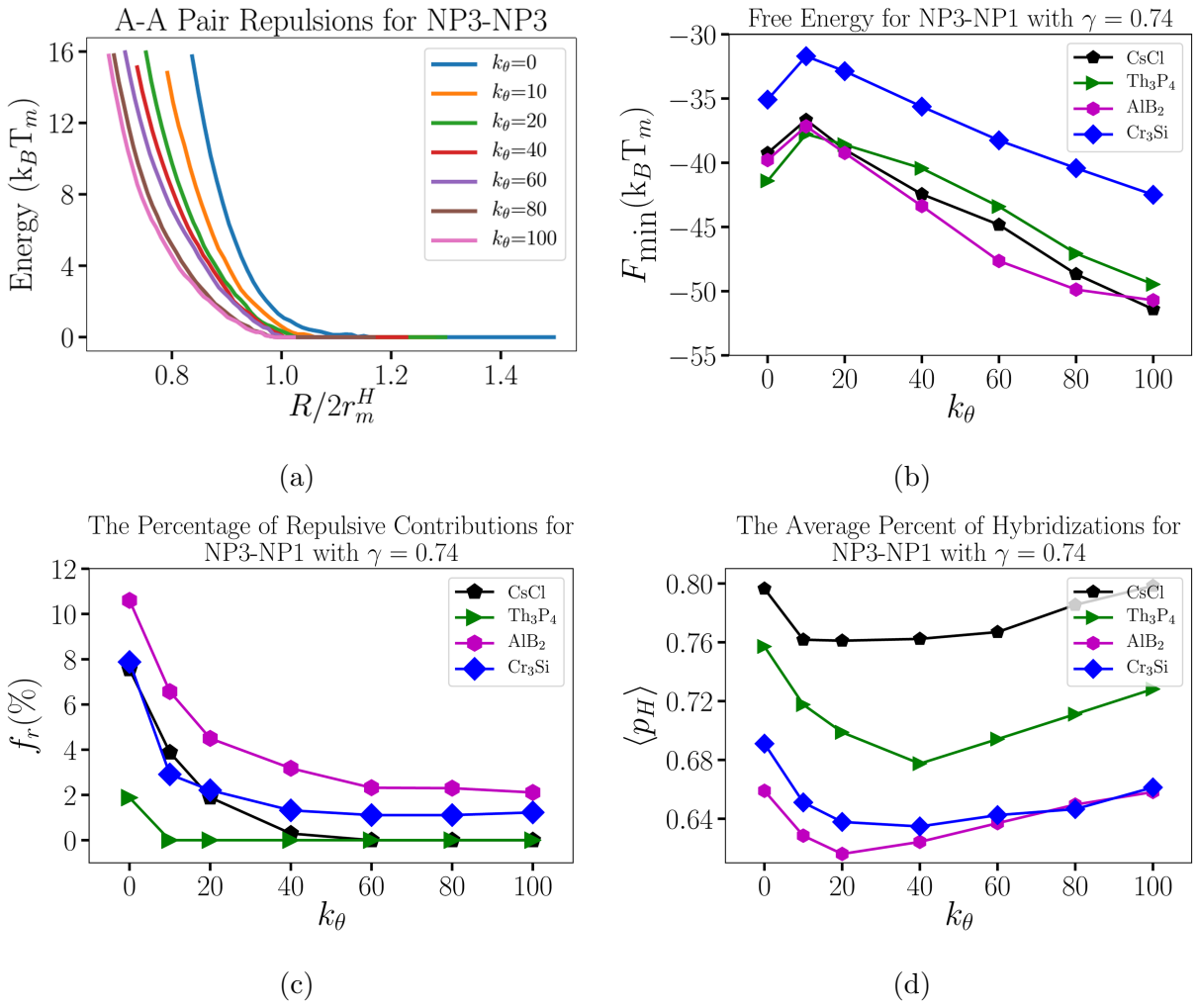

Figure 9: The effect of the spring parameter k_θ of the harmonic angle potential on (a) potential of mean force (NP3-NP3), (b) free energy, (c) the repulsive fraction f_r (see Eq. 17) and (d) the average percent of hybridizations $\langle p_H \rangle$ for CsCl, Th_3P_4, AlB_2 and Cr_3Si with $\gamma = 0.74$ (NP3 - NP1), see Table 2 for detailed values. All values are for $\frac{\varepsilon_{AB}}{k_BT_m} = 13.0$. The error bars are smaller in comparison to the symbol size.

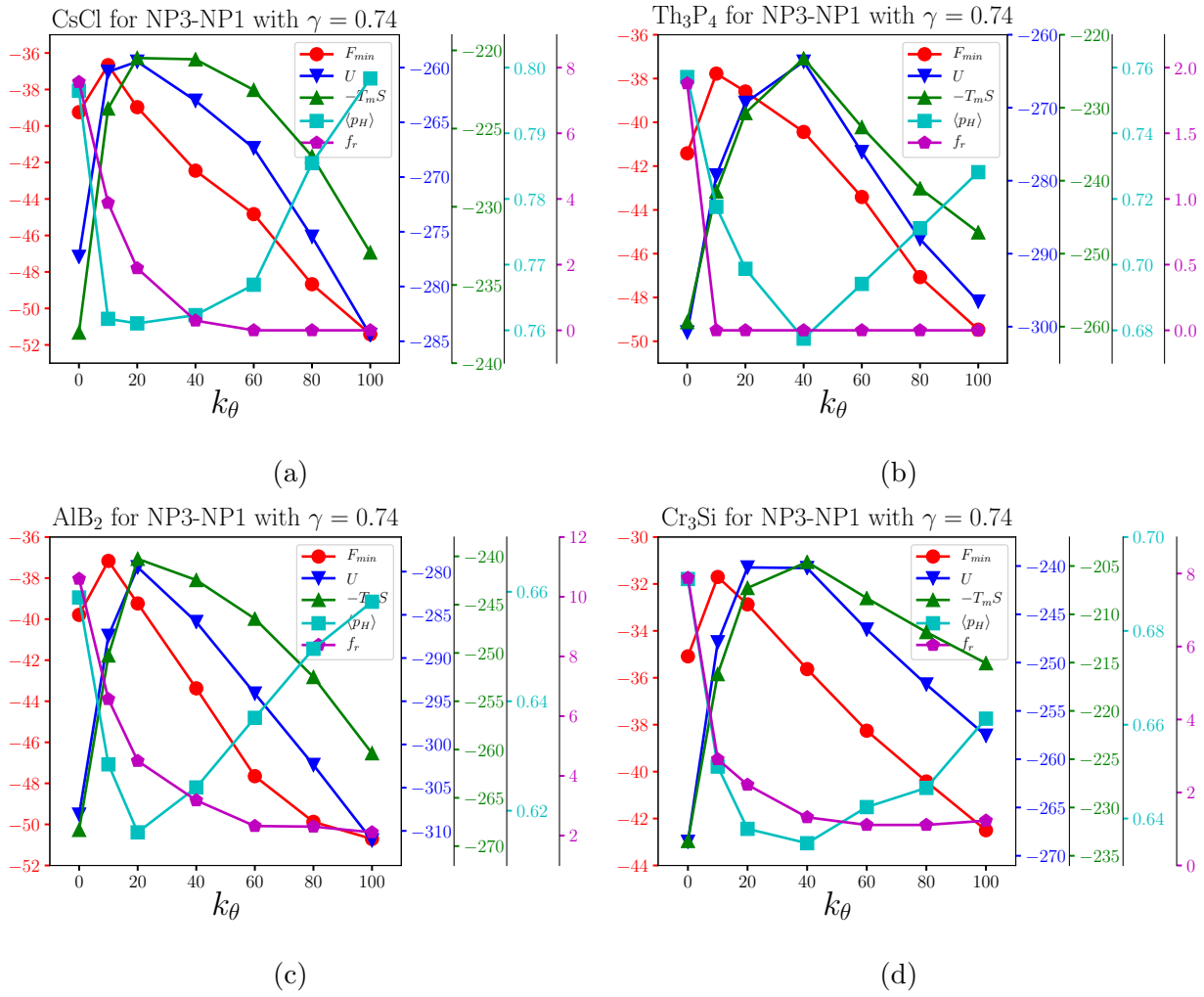

Figure 10: Free energies, internal energies, entropy, the average percent of hybridizations $\langle p_H \rangle$ and the repulsive fraction f_r vs the spring parameter k_θ of the harmonic angle potential for (a) CsCl, (b) Th_3P_4, (c) AlB_2 and (d) Cr_3Si with $\gamma = 0.74$ (NP3 - NP1), see Table 2 for detailed values. All values are for $\frac{\varepsilon_{AB}}{k_B T_m} = 13.0$. The units for the free energies, internal energies and -T_mS are all $k_B T_m$. The error bars are smaller in comparison to the symbol size.

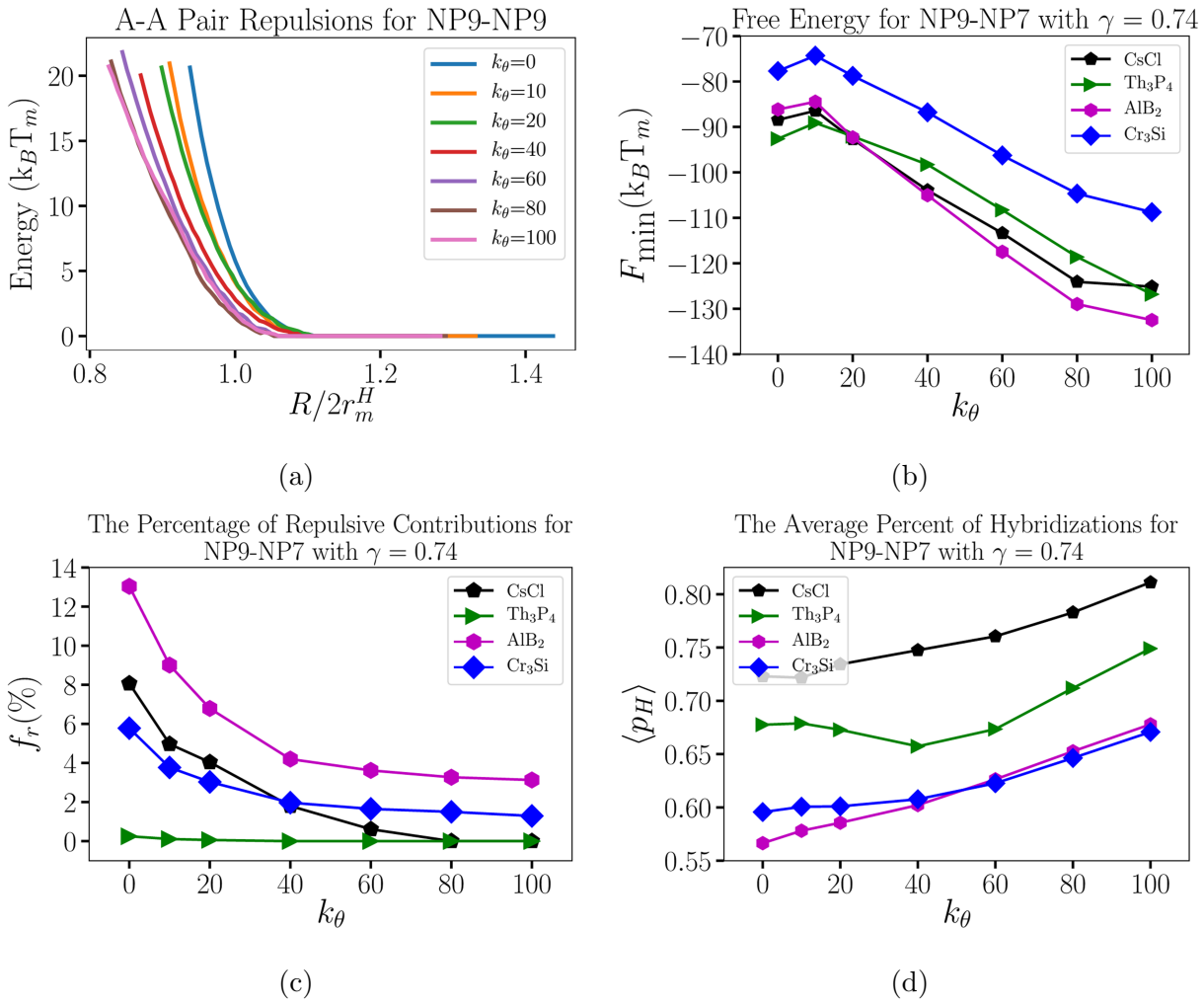

Figure 11: The effect of the spring parameter k_θ of the harmonic angle potential on (a) potential of mean force (NP9-NP9), (b) free energy, (c) the repulsive fraction f_r (see Eq. 17) and (d) the average percent of hybridizations $\langle p_H \rangle$ for CsCl, Th_3P_4, AlB_2 and Cr_3Si with $\gamma = 0.74$ (NP9 - NP7), see Table 2 for detailed values. All values are for $\frac{\varepsilon_{AB}}{k_BT_m} = 13.0$. The error bars are smaller in comparison to the symbol size.

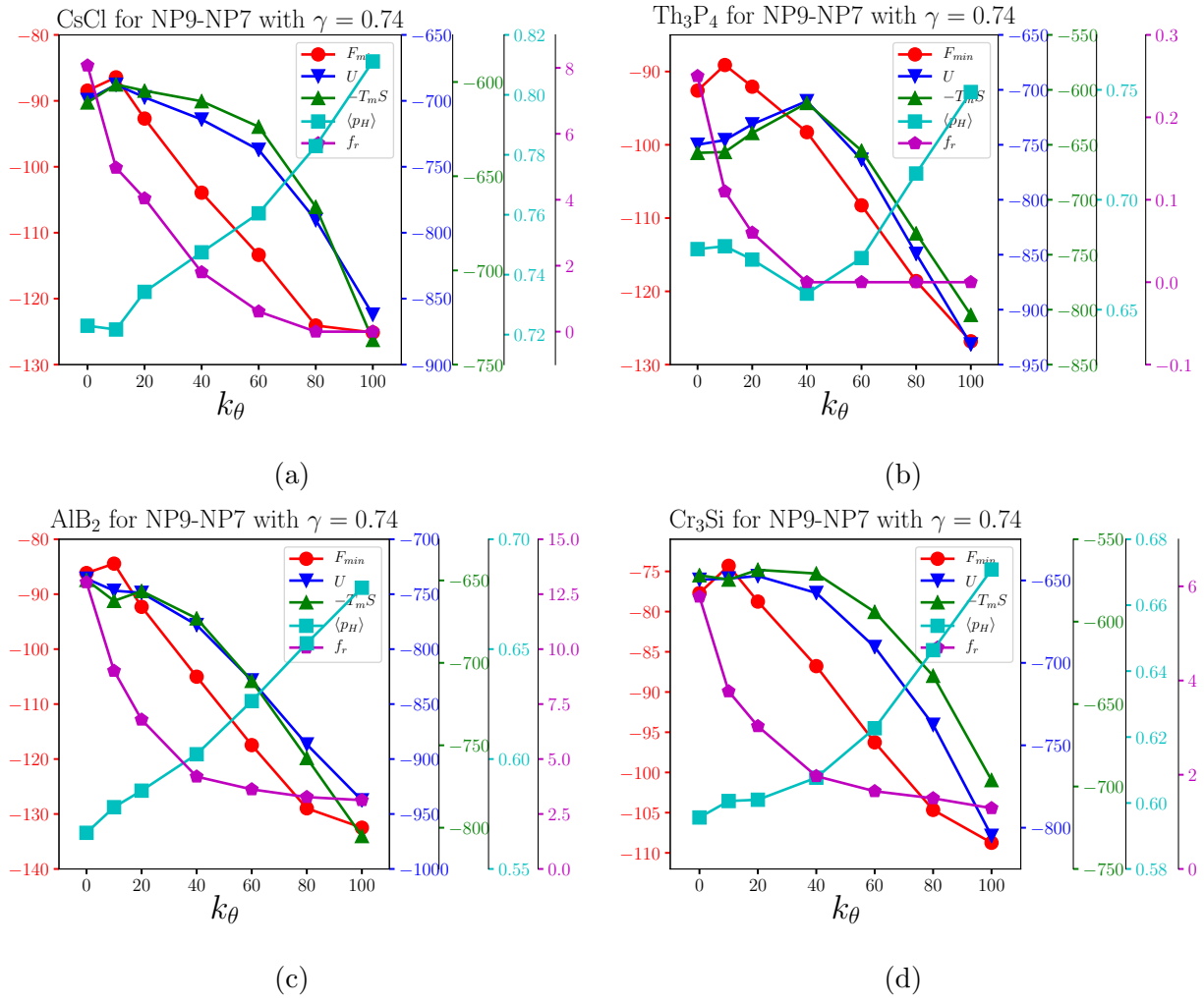

Figure 12: Free energies, internal energies, entropy, the average percent of hybridizations $\langle p_H \rangle$ and the repulsive fraction f_r vs the spring parameter k_θ of the harmonic angle potential for (a) CsCl, (b) Th_3P_4, (c) AlB_2 and (d) Cr_3Si with $\gamma = 0.74$ (NP9 - NP7), see Table 2 for detailed values. All values are for $\frac{\varepsilon_{AB}}{k_B T_m} = 13.0$. The units for the free energies, internal energies and -T_mS are all $k_B T_m$. The error bars are smaller in comparison to the symbol size.

Comparison to Experiment

Following the same practice as for DNA systems, we parameterize the phase diagrams in terms of the size ratio, parameterized with γ, see Eq. 6 and the linker ratio, that is, the

fraction of hydrogen bonds between A and B:

$$\text{Linker Ratio} = \frac{\sigma_{g,A} R_{c,A}^2}{\sigma_{g,B} R_{c,B}^2} \ . \tag{20}$$

The theoretical and experimental phase diagrams are established according to the corresponding simulated and experimental results, as shown in Figs. S18 and S19. Only within the range $\gamma \gtrsim 0.7$ BNSLs could systematically be assembled in experiments, and consist of either CsCl or Th_3P_4, in agreement with the previous reports.[15] Almost all $\gamma \lesssim 0.7$ lead to amorphous and/or unequilibrated systems, see Figs. S18(b) and S19(b).

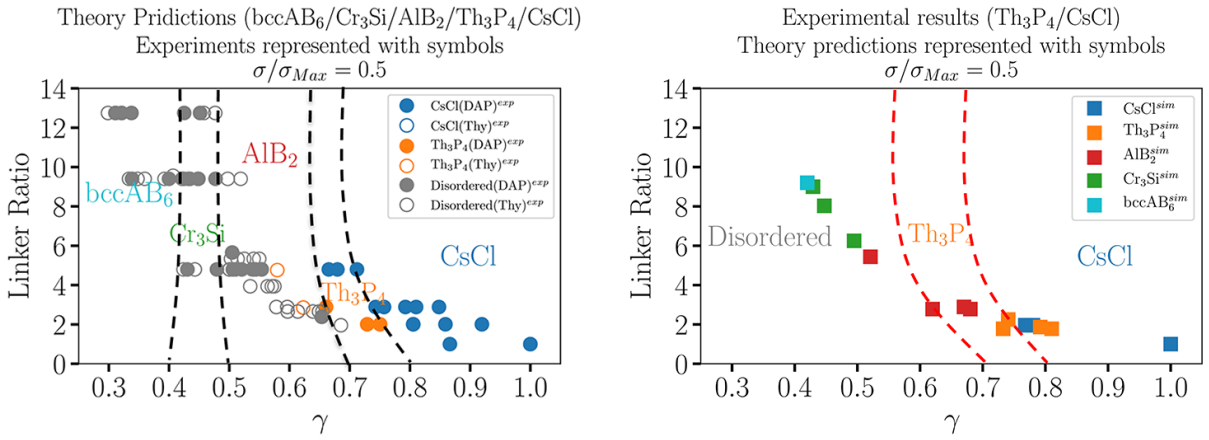

(a) (b)

Figure 13: (a) The theoretical phase diagram represented with dashed lines where the experiment results represented with circle symbols are added. (b) The experimental phase diagrams (flexible ligands $k_\theta = 0$, see Eq. 19) with $\sigma_g/\sigma_{g,Max} = 0.5$ and the PS coverage ratios (large to small NCT), where the black dashed lines are phase boundaries with the theoretical results represented with filled square symbols. DAP and Thy in brackets indicate that the NCTs with DAP or Thy are A particles. Definition of γ is given in Eq. 6 and Linker Ratio in Eq. 20.

In order to more clearly show the theory/experiment connection, we placed experimental results on the phase diagram predicted by theory and vice versa, see Fig. 13. For NCTs there is a general agreement between the theoretical and experimental phase diagrams about the sequence CsCl $\rightarrow$ Th_3P_4 and the location of the boundary between the two, but the experimental phase diagram is slightly shifted to the right except for the smallest linker

ratios. There are two experimental points in Fig. 13(a) that appear in a region that theory predicts should be AlB_2, i.e., the two orange empty circles. They correspond to samples 1-40 and 1-41 in Fig. S22. We have re-analyzed those cases on whether there is evidence for higher disorder, as compared from the cases that are within the predicted region, but no clear conclusions emerged. This maybe the result of our inability to compute tie lines and establish coexistence, as discussed. In any case, it is apparent that the CsCl BNSLs are of higher quality (sharper and more Bragg peaks) than the Th_3P_4. The most important disagreement, however, is that for $\gamma \lesssim 0.7$ theory predicts the sequence of phases as in Eq. 18, but those are absent in the experiment, a point that we further elaborate in the conclusions.

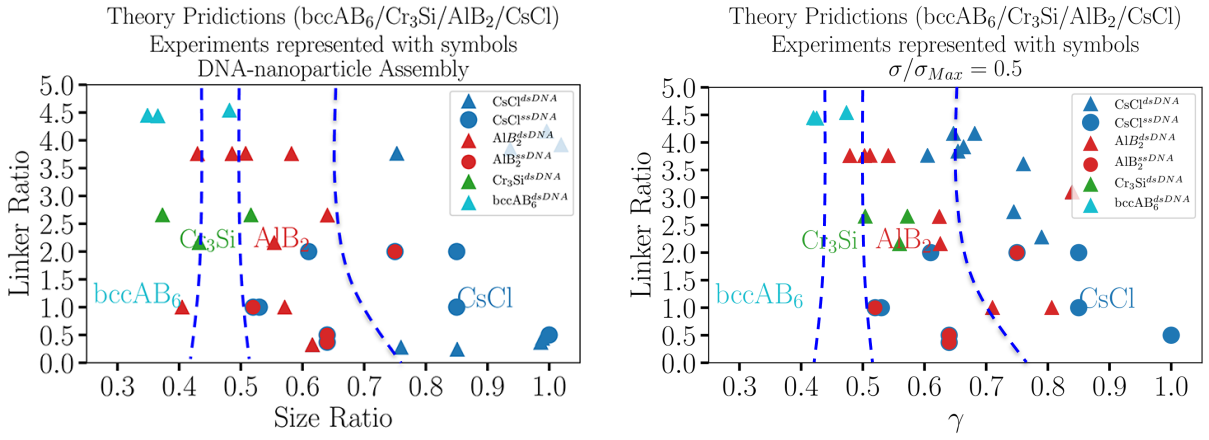

(a) (b)

Figure 14: (a) The theoretical phase diagrams as a function of (a) the hydrodynamic radius ratio, (b) the hard sphere radius ratio with $\sigma_g/\sigma_{g,Max} = 0.5$ and the dsDNA or ssDNA coverage ratios, where the black dashed lines are phase boundaries and "theory" in blue presents the theoretical phase diagram established by simulating BNSLs with NCTs grafted with finite rigidity ligand. The points are the experimental results collected from Ref.[6] and Ref.[20] dsDNA and ssDNA indicate the double or single stranded DNA. Definition of γ is given in Eq. 6 and that of Linker Ratio in Eq. 20.

For completeness, we establish the approximate theoretical phase diagram based on our study at finite rigidity, see Fig. 14. As indicated above, with increasing ligand rigidity, the Th_3P_4 BNSL is suppressed and the theoretical diagram boundary shifts to the right, which is supported by Figs. 9 and 11. In order to compare with theoretical prediction, we

provide the results with double stranded DNA (dsDNA) from Ref.[6] and also a few additional experiments with single stranded DNA (ssDNA) reported in Ref.[20] in Fig. 14, in terms of the original parameter (ratio of hydrodynamic radius) and also of γ, where we use the values for the maximum extension L provided in Ref.[6] The theoretical phase diagram is in fair agreement with these previous DNA experiments.

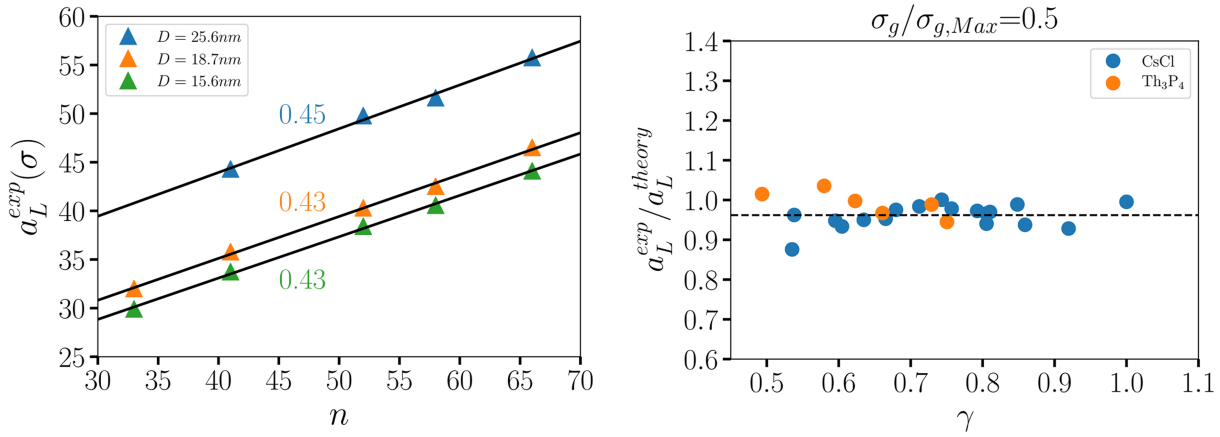

(a) (b)

Figure 15: (a) The variation of the experimental lattice constant with the chain length n for the bcc lattice with the core diameter D = 15.6, 18.7 and 26.5nm (see Table S14 and S15), where the black solid lines are the linear fitting; (b) The comparison of the measured lattice constant and the predicted values of the OPM formula by assuming $\sigma_g/\sigma_{g,Max} = 0.5$.

At a more quantitative level, in Fig. 15(a) we provide the dependence of the experimental lattice constant on the different theoretical parameters. Not only there is a linear dependence with the chain length n, see Fig. 6(d), but the predicted slope 0.36 is in fair agreement with the experimental results $0.43 - 0.45$. In Fig. 15(b) we compile all the lattice constants of the BNSLs as reported in experiments and compare them with the ones obtained from the OPM formula (assuming $\sigma_g/\sigma_{g,Max} = 0.5$), showing good agreement without the use of any fitting parameters. As shown in SI, see Fig. S17, the results are insensitive within small variations in grafting density, consistent with experiments.

Conclusions

Summary of Results

We have established the stability of five types of binary nanoparticle superlattices (BNSL): CsCl, Th_3P_4, AlB_2, Cr_3Si and bccAB$_6$ (Cs_6C_{60}) through rigorous free energy calculations and demonstrated that the ligand persistence length is a critical parameter; increasing ligand flexibility, the Th_3P_4 phase, see Fig. 9 for example, becomes stable as it minimizes the osmotic pressure exerted by neighboring (A-A, B-B) NCTs that cannot form hybridizations, as shown in Fig. 8. We have also determined that the phase diagram for binary DNA assembly[6] is a consequence of the long persistence length of the double stranded DNA. Although our study is focused on 3-dimensional BNSLs, the results may be extended to low-dimensional structures like cylinders and lamellae.[43]

Single stranded DNA has relatively small persistence length (≈ 1 nm[17]) compared with double stranded. There are previous studies aimed at establishing how this affects both the assembly dynamics and statics[44] at $\gamma = 1$. A prediction from our work is that single stranded DNA may include Th_3P_4 as well as the other superlattices in Eq. 18. Ref.[20] found that stoichiometry in conjunction with ratio of size and linker number determine the resulting equilibirium crystal structure in ssDNA-grafted nanoparticles. They reported a few instances of AlB_2 with the variation of stoichiometries from 1:1 to 1:2, see Fig. 14, besides CsCl, which overall match well our predictions. There have been other studies in related systems. For example, in Ref.[45] values of $\gamma < 1$ were explored, but they were close to one and consequently, only the CsCl was reported. A systematic study[46] of the role of the grafting density showed that binary systems, for sufficiently large grafting densities, do form superlattices over a putative amorphous gel, but here again, the values of γ were still not far from one, and consequently only CsCl was reported. A subsequent interesting study[47] did show that enhancing nanoparticle repulsion either gives raise to new phases, such as AuCl, or drives an instability into amorphous structures. The repulsion, however, is driven

by suppressing existing linkers, which is a different mechanism not considered here, so it is not possible to draw comparisons with our study. Hopefully, a systematic investigation of single stranded systems will provide further verification for the predictions presented here.

We have revealed that the dynamics of hybridization has universal (independent of molecular details) properties, as described by model independent power laws of the variable $y = e^{-\frac{\varepsilon_{AB}}{k_B T_m}}$, where ε_{AB} is the characteristic hybridization energy (more appropriately, free energy), see Fig. 5 for example. The exponential dependence provides a quantitative characterization of the strong temperature sensitivity of the assembly process as driven by hydrogen bonds. This knowledge will be exploited in the future work to optimize protocols for successful assembly, as discussed for example in Ref.,[48] with important implications in regards to highly asymmetric assemblies, $\gamma \lesssim 0.7$ (see Eq. 6), where our experiments, see Fig. 13, do not report BNSLs.

Connection to experiment

The theoretical predictions validated by experiments are:

- Stability of the Th_3P_4 phase, see Fig. 9b.
- Boundary between CsCl and Th_3P_4 phase, see Fig. 13.
- Lattice constant for all experiments (X-ray) see Fig. 15 For the actual value of the lattice constant, without fitting parameters.
- Hydrodynamic radius: see Fig. 2.

The experiments for slightly asymmetric nanoparticles $\gamma \gtrsim 0.7$ are in good agreement with theoretical predictions, not just in terms of the observed phases and their approximate regimes of stability, but also in their actual quantitative structure: lattice constants, dependence on number of monomers, etc.., see for example Fig. 15.

The most notable disagreement, however, is for highly asymmetric nanoparticles, where theory predicts several ordered phases, see Eq. 18 and the experiment turns is somewhat inconclusive and likely not properly equilibrated, indicating that future efforts to anneal these NCT systems out of kinetic traps must be explored. Further experiments in this region will be facilitated by our detailed understanding of the hybridization process, which will enable to test and design more sophisticated and efficient protocols to reach thermal equilibrium and establish whether the amorphous gel or the BNSL is the stable phase.

Nanocomposite Tectons as Unifying Systems

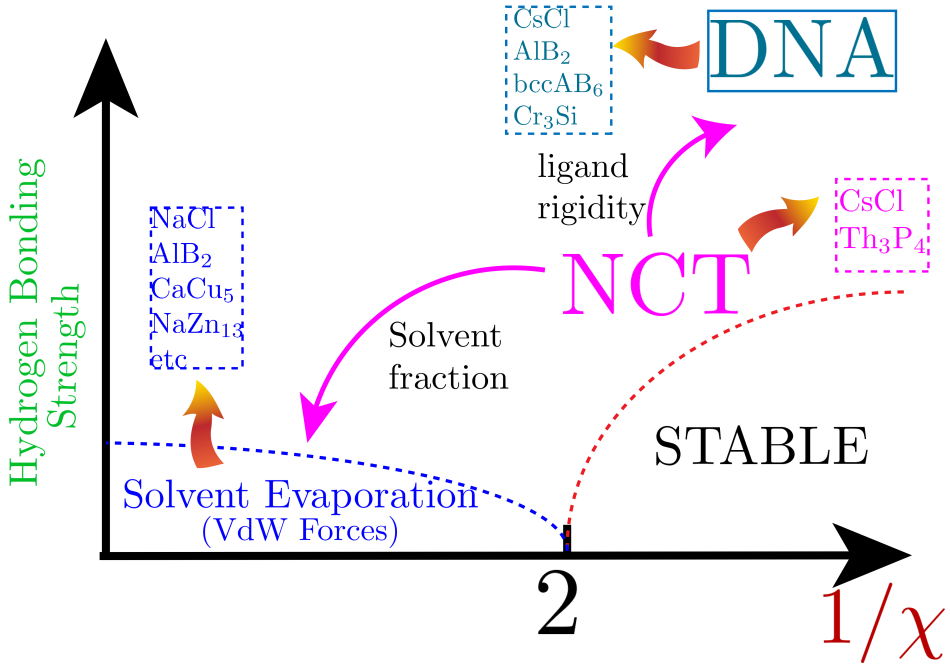

Figure 16: NCT leads to a unification of the most successful nanoparticle assembly methods.

The ability of NCTs to be stable in an organic solvent while forming hydrogen bonds allows them to regard them as a unifying assembly strategy, determined in terms of four parameters: Solvent quality χ, solvent fraction, ligand rigidity and hydrogen bonding strength. All successful BNSL assembly strategies reported so far in experiments can be described in terms of these four parameters.

A convenient way to illustrate the role of these four parameters is to describe solvent

quality (parameterized by the Flory-Huggins parameter χ) along the x-axis, for example polystyrene, ($\chi = \frac{1}{2}$ being the θ-point). The y-axis parameterizes the hydrogen bond strength between end moietes (e.g., Thy-DAP) relative to the thermal energy $|\frac{\varepsilon_H}{k_B T_m}|$. Fig. 16 illustrates that in good or θ solvent conditions ($\chi \leq \frac{1}{2}$) nanoparticles are stable, while $\chi >> \frac{1}{2}$ is akin to solvent evaporation, which in the absence of the hydrogen bonding, has been shown to lead to BNSLs[10] (although questions regarding their overall thermodynamic stability are still under some debate[28]).

Moving upwards in this parameter space, for good or θ conditions, sufficiently strong hydrogen bonding leads to the stability of the phases reported in DNA assembly,[6] with the addition of the Th_3P_4 phase depending on the persistence length of the ligands, as shown in Fig. 16. It is possible to continuously evolve from the previously obtained SE results to those observed for DNA directed assembly along this basic phase diagram, a possibility that has not been systematically explored.

In summary, our study shows how NCTs provide a certain unification for the most successful nanoparticle superlattice assembly strategies currently established: solvent evaporation and DNA programmable assembly. Future experimental and theoretical work should unravel additional phases and their possible novel properties.

Supporting Information Available

Supporting information contains one file with:

- *Force Field Parameters.*
- *Hybridization Characteristics.*
- *Analysis of γ.*
- *Effects of rigidity.*
- *Comparison to Experiment.*

- *Experimental Section.*
- *Brief Discussion on Solvent Quality.*

Acknowledgement

AT acknowledges discussions with L. Liz-Marzan, S. Mallapragada and D. Vaknin and specially O. Gang for a detailed clarification of his work. Nathan Horst work was funded by the Ames Laboratory, supported by the US Department of Energy, Basic Energy Sciences, Materials Science and Engineering Division, under Contract No. DE-AC02-07CH11358. The work of AT is funded by NSF, DMR-CMMT 1606336 "CDS&E: Design Principles for Ordering Nanoparticles into Super-crystals". This work used the Extreme Science and Engineering Discovery Environment (XSEDE), which is supported by National Science Foundation grant number ACI-1548562. Our project within XSEDE is supported by grant TG-MCB140071. HG also thanks for the support from NSF of China (21574142, 21790343) as well as the GPU Facility from Theoretical and Computational Chemistry Platform, Institute of Chemistry, Chinese Academy of Sciences. RJM acknowledges support from a NSF CAREER grant, award number CHE-1653289; the work was also supported in part by the US Army Research Office under grant W911NF-18-1-0197 and the Air Force Office of Scientific Research FA9550-17-1-0288; and made use of the MRSEC Shared Experimental Facilities at MIT, supported by the NSF under award DMR 14-19807. P.J.S. acknowledges support from the NSF Graduate Research Fellowship Program under grant NSF 1122374.

References

(1) Boles, M. A.; Talapin, D. V. Binary Assembly of PbS and Au Nanocrystals: Patchy PbS Surface Ligand Coverage Stabilizes the CuAu Superlattice. *ACS Nano* **2019**, *13*, 5375–5384.

(2) Alivisatos, A. P.; Johnsson, K. P.; Peng, X.; Wilson, T. E.; Loweth, C. J.; Bruchez, M. P.; Schultz, P. G. Organization of 'nanocrystal molecules' using DNA. *Nature* **1996**, *382*, 609–611.

(3) Mirkin, C. A.; Letsinger, R. L.; Mucic, R. C.; Storhoff, J. J. A DNA-based method for rationally assembling nanoparticles into macroscopic materials. *Nature* **1996**, *382*, 607–609.

(4) Nykypanchuk, D.; Maye, M. M.; van der Lelie, D.; Gang, O. DNA-guided crystallization of colloidal nanoparticles. *Nature* **2008**, *451*, 549–552.

(5) Park, S. Y.; Lytton-Jean, A. K. R.; Lee, B.; Weigand, S.; Schatz, G. C.; Mirkin, C. A. DNA-programmable nanoparticle crystallization. *Nature* **2008**, *451*, 553–556.

(6) Macfarlane, R. J.; Lee, B.; Jones, M. R.; Harris, N.; Schatz, G. C.; Mirkin, C. A. Nanoparticle Superlattice Engineering with DNA. *Science* **2011**, *334*, 204–208.

(7) Liu, W.; Tagawa, M.; Xin, H. L.; Wang, T.; Emamy, H.; Li, H.; Yager, K. G.; Starr, F. W.; Tkachenko, A. V.; Gang, O. Diamond family of nanoparticle superlattices. *Science* **2016**, *351*, 582.

(8) Shevchenko, E. V.; Talapin, D. V.; Murray, C. B.; O'Brien, S. Structural Characterization of Self-Assembled Multifunctional Binary Nanoparticle Superlattices. *Journal of the American Chemical Society* **2006**, *128*, 3620–3637.

(9) Shevchenko, E. V.; Talapin, D. V.; Kotov, N. A.; O'Brien, S.; Murray, C. B. Structural diversity in binary nanoparticle superlattices. *Nature* **2006**, *439*, 55–59.

(10) Ye, X.; Zhu, C.; Ercius, P.; Raja, S. N.; He, B.; Jones, M. R.; Hauwiller, M. R.; Liu, Y.; Xu, T.; Alivisatos, A. P. Structural diversity in binary superlattices self-assembled from polymer-grafted nanocrystals. *Nature Communications* **2015**, *6*, 10052.

(11) Hajizadeh, E.; Yu, S.; Wang, S.; Larson, R. G. A novel hybrid population balance—Brownian dynamics method for simulating the dynamics of polymer-bridged colloidal latex particle suspensions. *Journal of Rheology* **2018**, *62*, 235–247.

(12) Zhang, J.; Santos, P. J.; Gabrys, P. A.; Lee, S.; Liu, C.; Macfarlane, R. J. Self-Assembling Nanocomposite Tectons. *Journal of the American Chemical Society* **2016**, *138*, 16228–16231.

(13) Wang, Y.; Santos, P. J.; Kubiak, J. M.; Guo, X.; Lee, M. S.; Macfarlane, R. J. Multi-stimuli Responsive Nanocomposite Tectons for Pathway Dependent Self-Assembly and Acceleration of Covalent Bond Formation. *Journal of the American Chemical Society* **2019**, *141*, 13234–13243.

(14) Santos, P. J.; Cao, Z.; Zhang, J.; Alexander-Katz, A.; Macfarlane, R. J. Dictating Nanoparticle Assembly via Systems-Level Control of Molecular Multivalency. *Journal of the American Chemical Society* **2019**, *141*, 14624–14632.

(15) Santos, P. J.; Cheung, T. C.; Macfarlane, R. J. Assembling Ordered Crystals with Disperse Building Blocks. *Nano Letters* **2019**, *19*, 5774–5780.

(16) Santos, P. J.; Gabrys, P. A.; Zornberg, L. Z.; Lee, M. S.; Macfarlane, R. J. Macroscopic materials assembled from nanoparticle superlattices. *Nature* **2021**, *591*, 586–591.

(17) Knorowski, C.; Burleigh, S.; Travesset, A. Dynamics and statics of DNA-programmable nanoparticle self-assembly and crystallization. *Physical Review Letters* **2011**, *106*, 215501.

(18) Li, T. I.; Sknepnek, R.; Macfarlane, R. J.; Mirkin, C. A.; Olvera de la Cruz, M. Modeling the Crystallization of Spherical Nucleic Acid Nanoparticle Conjugates with Molecular Dynamics Simulations. *Nano Letters* **2012**, *12*, 2509–2514.

(19) Li, T.; Sknepnek, R.; De La Cruz, M. O. Thermally Active Hybridization Drives the Crystallization of DNA-Functionalized Nanoparticles. *Journal of the American Chemical Society* **2013**, *135*, 8535–8541.

(20) Vo, T.; Venkatasubramanian, V.; Kumar, S.; Srinivasan, B.; Pal, S.; Zhang, Y.; Gang, O. Stoichiometric control of DNA-grafted colloid self-assembly. *Proceedings of the National Academy of Sciences* **2015**, *112*, 4982–4987.

(21) Wang, M. X.; Brodin, J. D.; Millan, J. A.; Seo, S. E.; Girard, M.; Olvera De La Cruz, M.; Lee, B.; Mirkin, C. A. Altering DNA-Programmable colloidal crystallization paths by modulating particle repulsion. *Nano Letters* **2017**, *17*, 5126–5132.

(22) Thaner, R. V.; Eryazici, I.; Macfarlane, R. J.; Brown, K. A.; Lee, B.; Nguyen, S. B. T.; Mirkin, C. A. The Significance of Multivalent Bonding Motifs and "Bond Order"in DNA-Directed Nanoparticle Crystallization. *Journal of the American Chemical Society* **2016**, *138*, 6119–6122.

(23) Nayak, S.; Horst, N.; Zhang, H.; Wang, W.; Mallapragada, S.; Travesset, A.; Vaknin, D. Interpolymer Complexation as a Strategy for Nanoparticle Assembly and Crystallization. *The Journal of Physical Chemistry C* **2019**, *123*, 836–840.

(24) Horst, N.; Nayak, S.; Wang, W.; Mallapragada, S.; Vaknin, D.; Travesset, A. Superlattice assembly by interpolymer complexation. *Soft Matter* **2019**, *15*, 9690–9699.

(25) Travesset, A. Soft Skyrmions, Spontaneous Valence and Selection Rules in Nanoparticle Superlattices. *ACS Nano* **2017**, *11*, 5375–5382.

(26) Travesset, A. Topological structure prediction in binary nanoparticle superlattices. *Soft Matter* **2017**, *13*, 147–157.

(27) Xia, J.; Horst, N.; Guo, H.; Travesset, A. Superlattices of nanocrystals with polystyrene ligands: From the colloidal to polymer limit. *Macromolecules* **2019**, *52*, 39.

(28) Xia, J.; Guo, H.; Travesset, A. On the Thermodynamic Stability of Binary Superlattices of Polystyrene-Functionalized Nanocrystals. *Macromolecules* **2020**, *7*, 33.

(29) Bershtein, V. A.; Egorov, V. M. *Differential Scanning Calorimetry of Polymers: Physics, Chemistry, Analysis, and Technology.*; Ellis Horwood: New York, 1994.

(30) Zha, X.; Travesset, A. The Hard Sphere Diameter of Nanocrystals (Nanoparticles). *Journal of Chemical Physics* **2020**, *152*, 094502.

(31) Landman, U.; Luedtke, W. D. Small is different: energetic, structural, thermal, and mechanical properties of passivated nanocluster assemblies. *Faraday Discussions* **2004**, *125*, 1–22.

(32) Travesset, A. Phase diagram of power law and Lennard-Jones systems: Crystal phases. *The Journal of Chemical Physics* **2014**, *141*, 164501.

(33) Kumar, S.; Rosenberg, J. M.; Bouzida, D.; Swendsen, R. H.; Kollman, P. A. The weighted histogram analysis method for free-energy calculations on biomolecules. I. The method. *Journal of Computational Chemistry* **1992**, *13*, 1011–1021.

(34) Waltmann, C.; Horst, N.; Travesset, A. Capping Ligand Vortices as "atomic Orbitals" in Nanocrystal Self-Assembly. *ACS Nano* **2017**, *11*, 11273–11282.

(35) Anderson, J. A.; Lorenz, C. D.; Travesset, A. General purpose molecular dynamics simulations fully implemented on graphics processing units. *Journal of Computational Physics* **2008**, *227*, 5342–5359.

(36) Nguyen, T. D.; Phillips, C. L.; Anderson, J. A.; Glotzer, S. C. Rigid body constraints realized in massively-parallel molecular dynamics on graphics processing units. *Computer Physics Communications* **2011**, *182*, 2307–2313.

(37) Zha, X.; Travesset, A. Stability and Free Energy of Nanocrystal Chains and Superlattices. *The Journal of Physical Chemistry C* **2018**, *122*, 23153–23164.

(38) Glaser, J.; Zha, X.; Anderson, J. A.; Glotzer, S. C.; Travesset, A. Pressure in Rigid Body Molecular Dynamics. *Computational Materials Science* **2020**, *173*, 109430.

(39) Santos, P. J.; Macfarlane, R. J. Reinforcing Supramolecular Bonding with Magnetic Dipole Interactions to Assemble Dynamic Nanoparticle Superlattices. *Journal of the American Chemical Society* **2020**, *142*, 1170–1174.

(40) Bastús, N. G.; Comenge, J.; Puntes, V. Kinetically Controlled Seeded Growth Synthesis of Citrate-Stabilized Gold Nanoparticles of up to 200 nm: Size Focusing versus Ostwald Ripening. *Langmuir* **2011**, *27*, 11098–11105, PMID: 21728302.

(41) Yu, Q.; Shi, D.; Dong, W.; Chen, M. Optimizing the dynamic and thermodynamic properties of hybridization in DNA-mediated nanoparticle self-assembly. *Physical Chemistry Chemical Physics* **2021**, *23*, 11774–11783.

(42) Knorowski, C.; Travesset, A. Dynamics of DNA-programmable nanoparticle crystallization: Gelation, nucleation and topological defects. *Soft Matter* **2012**, *8*, 12053–12059.

(43) Zhu, G.; Xu, Z.; Yang, Y.; Dai, X.; Yan, L.-T. Hierarchical Crystals Formed from DNA-Functionalized Janus Nanoparticles. *ACS Nano* **2018**, *12*, 9467–9475, PMID: 30189141.

(44) Yu, Q.; Wang, R. Effect of Chain Rigidity on the Crystallization of DNA-Directed Nanoparticle System. *Macromolecules* **2018**, *51*, 8372–8376.

(45) Xiong, H.; van der Lelie, D.; Gang, O. Phase Behavior of Nanoparticles Assembled by DNA Linkers. *Physical Review Letters* **2009**, *102*, 015504.

(46) Zhang, Y.; Lu, F.; Yager, K. G.; van der Lelie, D.; Gang, O. A general strategy for the DNA-mediated self-assembly of functional nanoparticles into heterogeneous systems. *Nature Nanotechnology* **2013**, *8*, 865–872.

(47) Zhang, Y.; Pal, S.; Srinivasan, B.; Vo, T.; Kumar, S.; Gang, O. Selective transformations between nanoparticle superlattices via the reprogramming of DNA-mediated interactions. *Nature Materials* **2015**, *14*, 840–847.

(48) Mao, R.; Mittal, J. Self-assembly of DNA-functionalized nanoparticles guided by binding kinetics. *Journal of Physical Chemistry B* **2020**, *124*, 11593–11599.